
Study of Nature of Corona in Narrow Line Seyfert 1 Galaxies

Hiroshi H. IDOGAKI^{1*}, Shunichi OHMURA¹, Hiroaki TAKAHASHI², Shogo B. KOBAYASHI³, Yoshihiro UEDA¹, Yuichi TERASHIMA⁴, Kiyoshi HAYASHIDA², Takaaki TANAKA¹, Hiroyuki UCHIDA¹ and Takeshi Go TSURU¹

¹Department of Physics, Kyoto University, Kitashirakawa Oiwake-cho, Sakyo-ku, Kyoto 606-8502, Japan

²Department of Earth and Space Science, Osaka University, 1-1 Machikaneyama-cho, Toyonaka, Osaka 560-0043, Japan

³Department of Physics, Tokyo University of Science, 1-3 Kagurazaka, Shinjuku-ku, Tokyo 162-8601, Japan

⁴Department of Physics, Ehime University, 2-5 Bunkyo-cho, Matsuyama, Ehime, 790-8577, Japan

*E-mail: idogaki.hiroshi.47m@kyoto-u.jp

Received ; Accepted

Abstract

We study X-ray spectra of four Narrow Line Seyfert 1 galaxies (NLS1s), Mrk 110, SWIFT J2127.4+5654, IGR J16185–5928, and WKK 4438, using Suzaku and NuSTAR data. The spectra of the four sources are reproduced with a model consisting of a cutoff power law component, a reflection component, and a soft excess component. The photon indices of all the sources are found to be ~ 2 . The cutoff energies are constrained to be ~ 40 keV for Mrk 110, SWIFT J2127.4+5654, and WKK 4438, whereas a lower limit of 155 keV is obtained for IGR J16185–5928. We find that the NLS1s in our sample have systematically softer spectra and lower cutoff energies than Broad Line Seyfert 1 galaxies reported in the literature. We also perform spectral fittings with a model in which the cutoff power law is replaced with the thermal Comptonization model in order to directly obtain the electron temperature of the corona (kT_e). The fits give $kT_e \sim 10$ – 20 keV for Mrk 110 and SWIFT J2127.4+5654, and lower limits of $kT_e > 18$ keV for IGR J16185–5928 and $kT_e > 5$ keV for WKK 4438. We divide the NuSTAR data of SWIFT J2127.4+5654 into three periods according to the flux. The spectral fits in the three periods hint that kT_e is the lower in the higher flux period. The results of the four sources suggest a possible anti-correlation between kT_e and the ratio of the luminosity of Compton up-scattered photons to the Eddington luminosity. The anti-correlation can be explained by a simple model in which electrons in the corona are cooled and heated through inverse Compton scattering and Coulomb collisions with protons, respectively.

Key words: galaxies: active — galaxies: Seyfert — X-rays: galaxies

1 Introduction

Seyfert 1 galaxies (Sy1s) host Active Galactic Nuclei (AGNs), and are divided into two subclasses, Narrow Line Seyfert 1

galaxies (NLS1s) and Broad Line Seyfert 1 galaxies (BLS1s), based on the width of the $H\beta$ emission line (Osterbrock & Pogge 1985). According to the studies by e.g., Jin et al. (2012)

Table 1. Basic parameters of targets.

Object	Mrk 110	SWIFT J2127.4+5654	IGR J16185–5928	WKK 4438
Coordinates (J2000)	(09 ^h 25 ^m 12 ^s .9, +52°17′11″)	(21 ^h 27 ^m 44 ^s .9, +56°56′40″)	(16 ^h 18 ^m 36 ^s .4, -59°27′17″)	(14 ^h 55 ^m 16 ^s .7, -51°34′16″)
redshift z	0.0353	0.0147	0.0356	0.0160
N_{H} ($\times 10^{22}$ cm ⁻²)*	0.0133	0.770	0.216	0.291
M_{BH} ($\times 10^7 M_{\odot}$) [†]	1.8 [‡]	1.5 [§]	2.8	0.2

* the column density of Galactic interstellar medium

[†] the mass of SMBH[‡] Kollatschny (2004) [§] Malizia et al. (2008) ^{||} Masetti et al. (2006)**Table 2.** Observation logs.

Object	Date	ID	Exposure (ks)	Observatory
Mrk 110	2007/11/02	702124010	80	Suzaku
SWIFT J2127.4+5654	2007/12/09	702122010	82	Suzaku
	2012/11/04	60001110002	49	NuSTAR
	2012/11/05	60001110003	29	NuSTAR
	2012/11/06	60001110005	75	NuSTAR
	2012/11/08	60001110007	42	NuSTAR
IGR J16185–5928	2008/02/09	702123010	68	Suzaku
WKK 4438	2012/01/22	706011010	70	Suzaku

and Ai et al. (2013), NLS1s and BLS1s have similar bolometric luminosities L_{bol} ($\sim 10^{44-47}$ erg s⁻¹) although the SMBH mass of NLS1s is typically smaller ($M \sim 10^{6-7} M_{\odot}$). Thus, the Eddington ratios of NLS1s are generally higher than those of BLS1s, implying that NLS1s are in the early phase of the Super Massive Black Hole (SMBH) growth.

X-ray spectra of Sy1s are described roughly by a power law with a high energy cutoff at $\sim 10^{1-2}$ keV. The emission mechanism is supposed to be inverse Compton scattering, in which low energy photons from the accretion disk are up-scattered by thermal electrons in the accretion corona (Haardt et al. 1994). Some of the up-scattered photons are reflected (Compton down-scattered and photoelectrically absorbed) by surrounding matter (George & Fabian 1991) such as the dusty torus and/or the disk. These reflected photons produce the common features such as the Compton hump as well as the Fe K α emission line and the Fe K α edge.

Malizia et al. (2003) studied hard X-ray spectra of nine BLS1s, analyzing data obtained with the BeppoSAX MECS and PDS. They combined spectra of the nine BLS1s, and obtained a cutoff energy of $E_c = 216_{-41}^{+75}$ keV. Malizia et al. (2008) carried out a similar analysis for five NLS1s with the Swift XRT and the INTEGRAL IBIS, and obtained $E_c = 38_{-10}^{+17}$ keV. Since $E_c \approx 2-3kT_e$ (Petrucci et al. 2001), the results by Malizia et al. (2003, 2008) imply that NLS1s have lower electron temperatures than BLS1s. Malizia et al. (2008) claimed that the higher accretion rate of NLS1s enhances Compton up-scattering, and that the corona of NLS1s does not have a temperature as high as that of BLS1s.

For individual sources, Malizia et al. (2014) performed 0.3–100 keV spectral analysis of 41 BLS1s included in the INTEGRAL complete sample of AGNs. They had 26 measure-

ments of the cutoff distributed between 50 and 200 keV with the mean value of the cutoff energies of $E_c = 128$ keV, which corresponds to $kT_e \sim 50$ keV. Although these measurements were all assuming a phenomenological cutoff power law model to determine the spectral cutoff, a recent study by Tortosa et al. (2018) directly determined the electron temperatures of two BLS1s, MCG +8–11–11 and NGC 6814, with NuSTAR by utilizing a Comptonization model as 60_{-30}^{+110} keV and 45_{-17}^{+100} keV, respectively. As for NLS1s, several studies have been carried out to characterize the properties of individual sources in the hard X-ray band (Malizia et al. 2008; Kara et al. 2017; Marinucci et al. 2014; Miniutti et al. 2009; Patrick et al. 2011; Panessa et al. 2011). In addition to well-studied SWIFT J2127.4+5654, cutoff energies of three NLS1s have been successfully determined so far by those authors.

In this paper, we study spectra of four NLS1s obtained with Suzaku (Mitsuda et al. 2007) and NuSTAR (Harrison et al. 2013) in order to measure their cutoff energies and characterize the properties of the corona. Throughout this paper, the Hubble constant $H_0 = 70$ km s⁻¹ Mpc⁻¹ is adopted. Errors are quoted at 90% confidence levels in the text and tables, and error bars in the figures indicate 1σ confidence intervals.

2 Observations and Data Reduction

As the targets of the present study, we selected Mrk 110, SWIFT J2127.4+5654, IGR J16185–5928, and WKK 4438, which have relatively high flux ($\gtrsim 10^{-11}$ erg s⁻¹ cm⁻² in 14–195 keV band) in the Swift BAT 58 months catalog (Baumgartner et al. 2010) to study the properties in the hard X-ray band and obtain cutoff energies. Their basic parameters and the observation logs are summarized in tables 1 and 2, re-

spectively.

2.1 Suzaku Observations

The Suzaku observations were carried out with the X-ray Imaging Spectrometer (XIS; Koyama et al. 2007) and the Hard X-ray Detector (HXD; Takahashi et al. 2007; Kokubun et al. 2007). The XIS consists of four CCD cameras: three (XIS0, XIS2, XIS3) with front-illuminated (FI) CCDs and one (XIS1) with a back-illuminated (BI) CCD. We did not use XIS2 because it had been out of function since 2006. The XIS0 data of SWIFT J2127.4+5654 are not available because of a trouble in on-board data processing. The normal full-window clocking mode with the spaced-row charge injection (Ozawa et al. 2009; Uchiyama et al. 2009) was employed.

We reprocessed the XIS and HXD datasets by using the Calibration Database (CALDB) released in 2016 April and reduced them by using the HEASOFT package version 6.18. We employed the same data-selection criteria as those used for the archived cleaned event lists. We analyzed the data in the time intervals in which both the XIS and HXD data were simultaneously available.

Each XIS source spectrum was extracted from circular regions with a $3'$ radius centered at the source. The background was taken from off-source circular regions with a $3'$ radius for Mrk 110, SWIFT J2127.4+5654, and IGR J16185–5928, which were observed at the HXD nominal position. WKK 4438 was observed at the XIS nominal position, which makes it difficult to select a background region in the above mentioned manner. Thus, the background for WKK 4438 was taken from an annular region with inner and outer radii of $3'$ and $6'$, respectively. The redistribution matrices and the ancillary response files were made for each XIS spectra using `xisrmfgen` and `xissimarfgen`, respectively.

We followed the standard data reduction procedure for the HXD-PIN data. For the HXD-PIN Non X-ray Background (NXB), we used simulated event files supplied by the HXD team based on the LCFITDT model (Fukazawa et al. 2009), which is estimated to have 1σ systematic errors less than 3% in the 15–40 keV band. The Cosmic X-ray Background (CXB) component was simulated by assuming the empirical model by Boldt (1987). We simulated the CXB component with this spectral model and the HXD response file for a uniform diffuse emission, and added to the NXB component to make the total background spectrum. In the spectral analysis, we used the HXD-PIN response files, `ae_hxd_pinhxnome4_20080129.rsp` and `ae_hxd_pinhxnome11_20110601.rsp` for the HXD nominal position and XIS nominal position, respectively.

2.2 NuSTAR Observation

The NuSTAR observation of SWIFT J2127.4+5654 was carried out with Focal Plane Module A (FPMA) and B (FPMB), which consist of CdZnTe pixel detectors. We reprocessed the data by using the CALDB released in 2017 May and reduced them by using the HEASOFT package version 6.21. We then extracted high-level scientific products from cleaned Level 2 “01” event files by using `nuproducts`. The source spectra were extracted from a circular region with a $1.9'$ radius centered at the source, and the background was extracted from an off-source circular region with a $1.9'$ radius.

3 Spectral Analysis and Results

3.1 Suzaku Analysis

We analyzed time averaged spectra of the four NLS1s by using XSPEC (Arnaud 1996). The cross-normalization factor of the HXD-PIN with respect to FI-XIS was set to 1.16 for the XIS nominal position observation and 1.18 for the HXD nominal position observations by referring to Suzaku Memo¹. In order to grasp overall spectral shape, we first used a single power law model absorbed by interstellar medium (`phabs` in XSPEC). In order to avoid the influence of the structures commonly seen in the spectra of NLS1s such as the soft excess, the Compton hump, and the Fe $K\alpha$ emission line, the model was applied to the 2.5–12 keV energy band excluding 4.5–7.5 keV. The absorption column densities were fixed to the Galactic values taken from the results of the Leiden/Argentine/Bonn Survey (Kalberla et al. 2005) in the following analyses. Figure 1 shows the spectral ratios between the data in the 0.3–40 keV energy band and the model. The fits gave photon indices Γ in the range of 1.7–2.0. We found cutoff features around 20 keV in the spectra of Mrk 110, SWIFT J2127.4+5654, and WKK 4438. Emission line features are found in all the sources around 6.4 keV in rest frame energy.

The detection of the emission lines at ~ 6.4 keV provides evidence of reflection on cold matter such as the dusty torus. We, therefore, applied the `pexrav` model introduced by Magdziarz & Zdziarski (1995), which represents an exponentially cut-off power law component and its reflection continuum. The emission line from cold matter was separately described by a Gaussian model (`zgauss`). Hereafter, the inclination angle was fixed to 60° and the abundance of elements in accreting matter was assumed to be solar. The normalization of the reflection component is represented by the reflection fraction of $R \equiv \Omega/(2\pi)$, where Ω is the solid angle of the reflector viewed from the X-ray source. Since figure 1 shows that Mrk 110 and IGR J16185–5928 have significant soft excess components, a blackbody model (`zbody`) was added to phenomenologi-

¹ (<ftp://legacy.gsfc.nasa.gov/suzaku/doc/xrt/suzakumemo-2008-06.pdf>).

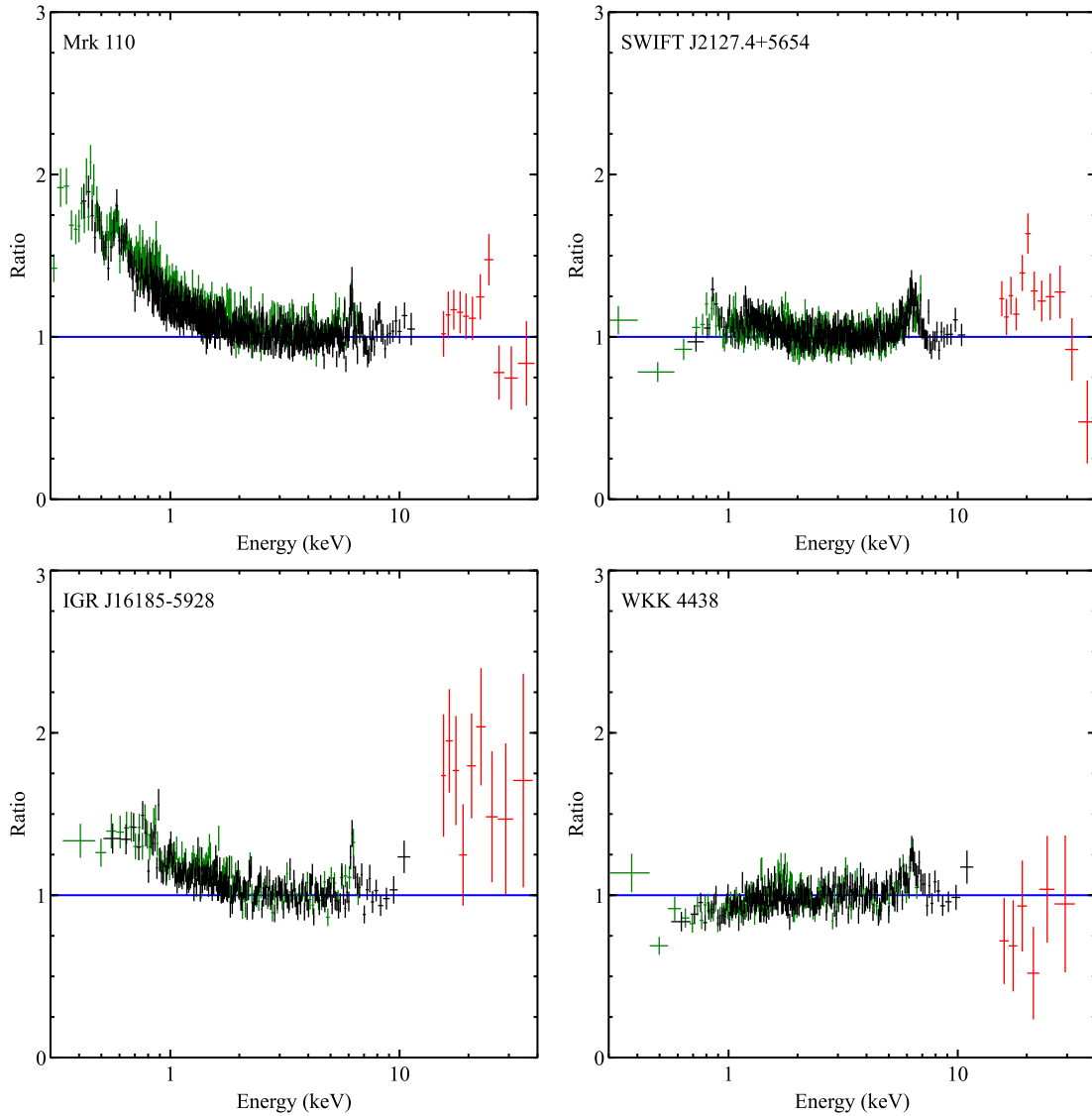


Fig. 1. Ratios of the spectra of Mrk 110, SWIFT J2127.4+5654, IGR J16185–5928, and WKK 4438 to power law models. The black, green, and red crosses correspond to FI-XIS, BI-XIS, and HXD-PIN, respectively.

cally represent the structures. Although SWIFT J2127.4+5654 and WKK 4438 do not display particularly strong soft excess emission, the fits were improved by including the blackbody model compared with the fits without the blackbody model with $\Delta\chi^2$ of 13.2 and 29.3 for SWIFT J2127.4+5654 and WKK 4438. They correspond to the F-test significance levels of $\sim 3\sigma$ and $\sim 4\sigma$, respectively. Thus, we added `zbody` to the model for SWIFT J2127.4+5654 and WKK 4438 as well as the other two sources. We also checked the presence of the intrinsic absorption in the sources by adding the model of the photoelectric absorption `zphabs` and found no significant additional absorption with the upper limits of 4×10^{18} , 6×10^{20} , 8×10^{20} and $4 \times 10^{20} \text{ cm}^{-2}$ for Mrk 110, SWIFT J2127.4+5654, IGR J16185–5928, and WKK 4438, respectively. We show the results of the spectral fits with the

model `phabs*(pexrav+zgauss+zbody)` (model A) in figure 2 and summarize the best-fit parameters in table 3. We confirmed that the line centroids of the emission line are consistent with that of the neutral Fe $K\alpha$ line at 6.4 keV. The cutoff energies E_c are ~ 40 keV for Mrk 110, SWIFT J2127.4+5654, and WKK 4438. The lower limit of $E_c > 155$ keV was obtained for IGR J16185–5928.

The continuum described by a cutoff power law can be ascribed to Compton up-scattering of seed photons by accreting electrons (Haardt et al. 1994). The cutoff energy is related to the electron temperature kT_e as $E_c \approx 2-3kT_e$ (Petrucci et al. 2001). In order to directly obtain kT_e from spectral fittings, we used the thermal Comptonization model (`nthcomp`; Zdziarski et al. 1996; Życki et al. 1999) instead of the `pexrav` model, and the convolution model for reflection on cold matter (`reflect`; Magdziarz

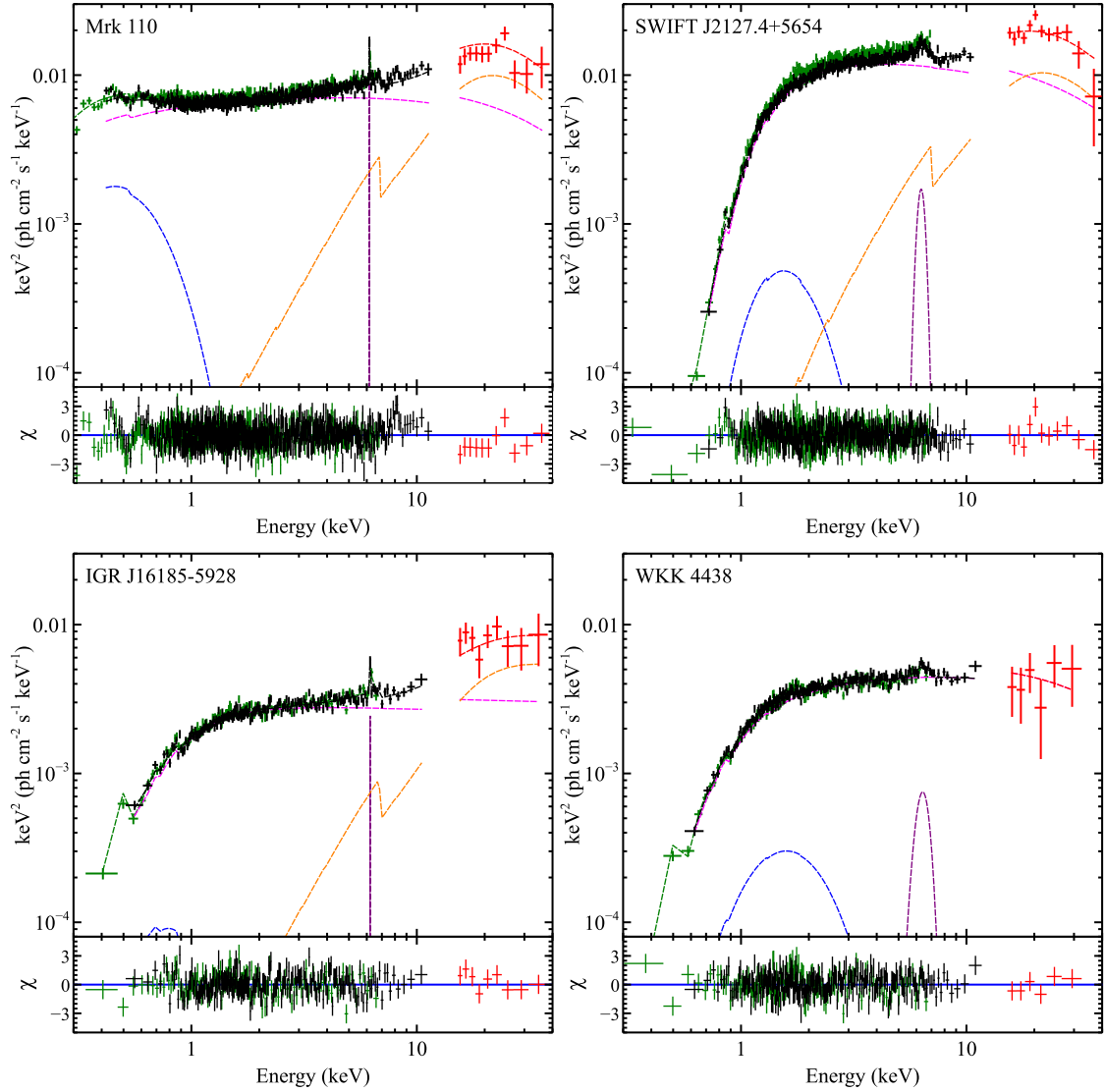


Fig. 2. Results of the spectral fits of Mrk 110, SWIFT J2127.4+5654, IGR J16185–5928, and WKK 4438 with model A. The crosses are the same as figure 1, and the dashed lines represent the models. The magenta, orange, purple, and blue lines correspond to the cutoff power law, reflection on cold matter, Fe emission line, and soft X-ray excess component, respectively.

Table 3. Best-fit parameters with model A.

Model	Parameter	Mrk 110	SWIFT J2127.4+5654	IGR J16185–5928	WKK 4438
pexrav	Γ	1.84 ± 0.02	2.01 ± 0.05	2.04 ± 0.03	$1.79^{+0.05}_{-0.06}$
	E_c (keV)	35^{+10}_{-6}	38^{+23}_{-9}	> 155	35^{+30}_{-16}
	Normalization*	$(6.3 \pm 0.1) \times 10^{-3}$	$(1.3 \pm 0.1) \times 10^{-2}$	$(3.0 \pm 0.1) \times 10^{-3}$	$(3.5 \pm 0.1) \times 10^{-3}$
	R	2.7 ± 0.6	2.2 ± 0.9	$2.6^{+0.7}_{-0.6}$	< 3.3
zgauss	Line energy (keV)	6.38 ± 0.03	6.37 ± 0.09	$6.43^{+0.04}_{-0.03}$	6.43 ± 0.14
	Line width (keV)	< 0.08	$0.26^{+0.19}_{-0.13}$	< 0.08	< 0.66
	Normalization*	$(0.9 \pm 0.3) \times 10^{-5}$	$(2.8^{+2.0}_{-1.3}) \times 10^{-5}$	$(6.0^{+2.1}_{-1.8}) \times 10^{-6}$	$(2.2 \pm 0.9) \times 10^{-5}$
	Equivalent width (eV)	35 ± 10	77^{+39}_{-35}	64^{+24}_{-25}	192 ± 45
zbody	kT_{bb} (keV)	0.11 ± 0.01	$0.27^{+0.03}_{-0.02}$	$0.13^{+0.03}_{-0.02}$	$0.35^{+0.05}_{-0.04}$
	Normalization*	$(5.7 \pm 0.5) \times 10^{-5}$	$(3.4 \pm 1.5) \times 10^{-5}$	$(1.1 \pm 0.6) \times 10^{-5}$	$(1.1^{+0.4}_{-0.3}) \times 10^{-5}$
χ^2/dof		1134.85/972	735.19/717	379.43/329	446.74/375

* in units of $\text{ph keV}^{-1} \text{cm}^{-2} \text{s}^{-1}$.

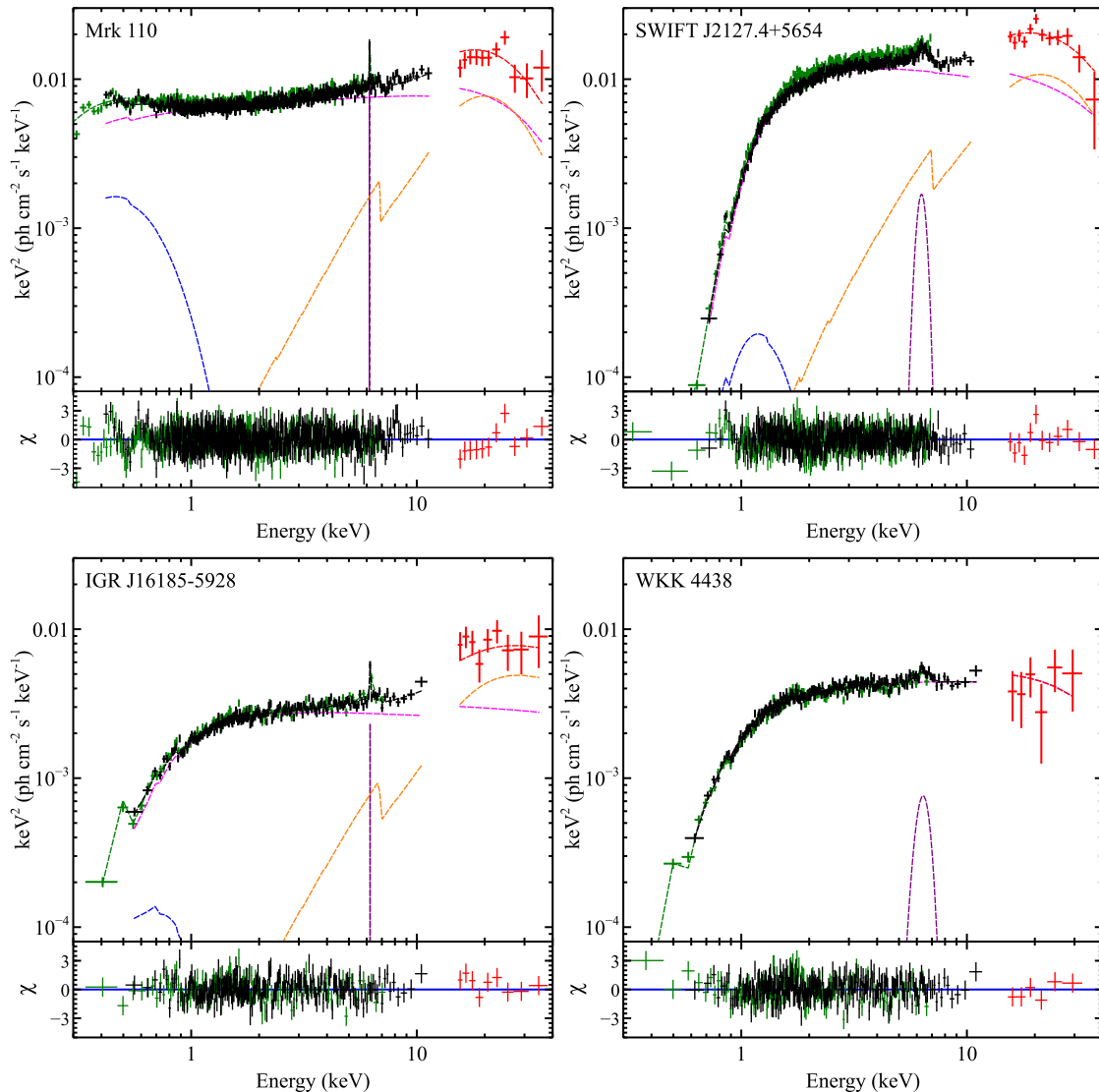


Fig. 3. Results of the spectral fits of Mrk 110, SWIFT J2127.4+5654, IGR J16185–5928, and WKK 4438 with model B. The crosses and lines are the same as figure 2 but the magenta lines represent the thermal Comptonization component.

& Zdziarski 1995). The seed photon temperature kT_s was assumed to be the same as the blackbody temperature kT_{bb} of the zbody model. The results of the spectral fits with the model `phabs*[(1+reflect)*nthcomp+zgauss+zbody]` (model B) are shown in figure 3 and the best-fit parameters are in table 4. While we assumed the source of the Compton seed photons, namely the soft excess, to be a blackbody, some alternative interpretations are proposed by several authors as well. For example, some claimed that the soft excess can be explained as the hardest end of a Comptonized accretion disk emission which is originated from an additional cool and thick corona (e.g., Done et al. 2012, 2013; Jin et al. 2012; Petrucci et al. 2013). If this is the case, kT_s could be overestimated/underestimated in our analysis. Thus, the assumption on kT_s is rather model dependent. Therefore, we also fit the spectra allowing kT_s to

vary as a free parameter independent of kT_{bb} . The upper limit or best-fit values for kT_s were < 0.06 , $0.15^{+0.09}_{-0.02}$, $0.20^{+0.03}_{-0.12}$, and 0.14 ± 0.01 keV for Mrk 110, SWIFT J2127.4+5654, IGR J16185–5928, and WKK 4438, respectively. They are equivalent with (SWIFT J2127.4+5654, IGR J16185–5928, and WKK 4438) or slightly lower (Mrk 110) than kT_{bb} . In addition, we found that the fits do not significantly change the other parameters given in table 4, in particular kT_e and Γ which are the key parameters for the main subject of this paper. Hence, we hereafter show only the results obtained under the assumption that kT_s is equivalent to kT_{bb} for simplicity.

In our sample, WKK 4438 has a relatively weak reflection continuum with the reflection fractions of $R < 0.4$. On the other hand, Mrk 110, SWIFT J2127.4+5654, and IGR J16185–5928 exhibit a high reflection fractions of $R \sim 2$. The high R

Table 4. Best-fit parameters with model B.

Model	Parameter	Mrk 110	SWIFT J2127.4+5654	IGR J16185–5928	WKK 4438
nthcomp	Γ	1.92 ± 0.02	2.13 ± 0.04	$2.05^{+0.03}_{-0.04}$	$1.95^{+0.02}_{-0.01}$
	kT_e (keV)	$7.4^{+0.8}_{-0.7}$	11^{+5}_{-2}	> 18	> 5
	Normalization*	$(6.4 \pm 0.1) \times 10^{-3}$	$(1.4 \pm 0.1) \times 10^{-2}$	$(3.0 \pm 0.1) \times 10^{-3}$	$(3.9 \pm 0.1) \times 10^{-3}$
reflect	R	2.1 ± 0.4	$2.3^{+1.0}_{-0.8}$	$2.7^{+0.7}_{-0.8}$	< 0.4
zgauss	Line energy (keV)	6.38 ± 0.03	$6.36^{+0.09}_{-0.11}$	6.42 ± 0.04	6.43 ± 0.14
	Line width (keV)	< 0.08	0.3 ± 0.2	< 0.09	0.5 ± 0.2
	Normalization*	$(0.9 \pm 0.3) \times 10^{-5}$	$(3.5^{+2.2}_{-1.7}) \times 10^{-5}$	$< 6.5 \times 10^{-6}$	$(2.2^{+0.8}_{-0.7}) \times 10^{-5}$
	Equivalent width (eV)	36 ± 10	94^{+40}_{-38}	< 61	199^{+204}_{-81}
zbody	kT_{bb} (keV)	0.099 ± 0.003	$0.16^{+0.02}_{-0.04}$	0.11 ± 0.01	0.14 ± 0.01
	Normalization*	$(8.2 \pm 0.53) \times 10^{-5}$	$< 7.6 \times 10^{-5}$	$(2.3 \pm 0.7) \times 10^{-5}$	$< 0.1 \times 10^{-5}$
	$F_{0.3-40 \text{ keV}}$ (erg cm $^{-2}$ s $^{-1}$) †	8.9×10^{-11}	8.7×10^{-11}	2.9×10^{-11}	2.8×10^{-11}
	$L_{0.3-40 \text{ keV}}$ (erg s $^{-1}$) †	2.4×10^{44}	4.1×10^{43}	8.0×10^{43}	1.5×10^{43}
	F_{Comp} (erg cm $^{-2}$ s $^{-1}$) ‡	5.3×10^{-11}	8.8×10^{-11}	$> 2.3 \times 10^{-11}$	$> 2.7 \times 10^{-11}$
	L_{Comp} (erg s $^{-1}$) ‡	1.4×10^{44}	4.1×10^{43}	$> 6.3 \times 10^{43}$	$> 1.5 \times 10^{43}$
	χ^2/dof	1129.27/972	735.74/717	358.94/329	458.36/375

* in units of ph keV $^{-1}$ cm $^{-2}$ s $^{-1}$.

† absorbed flux or luminosity in 0.3–40 keV.

‡ unabsorbed flux or luminosity of the Comptonized component.

value suggests possible contributions from additional reflection components. Since Fe K α emission lines in Mrk 110 and IGR J16185–5928 are narrow, the additional component should be cold similarly to the dusty torus and, therefore, would be attributed to the outer part of the accretion disk. In contrast to the two sources, we detected a broad Fe K α emission line in the SWIFT J2127.4+5654 spectrum, as already reported by Miniutti et al. (2009) and Patrick et al. (2011), which provides firm evidence of the reflection component from the inner part of the accretion disk. This is because the broad emission line is considered to be due to relativistic effects such as Doppler motions and gravitational redshifts (Fabian et al. 1989) and/or many unresolved lines from various ionization states (Ross & Fabian 1993).

We added to the SWIFT J2127.4+5654 spectrum a reflection continuum model in which a thermal Comptonization model (nthcomp) is convolved with the model simulating the relativistic effects (kdblur; Laor 1991) and also with the ionized reflection model (ireflect; Magdziarz & Zdziarski 1995). The outer disk radius was assumed to be $400r_g$, the value Patrick et al. (2011) fixed to, where r_g is the gravitational radius. In accordance with the result by Patrick et al. (2011), the inner disk radius and the radial emissivity index of the disk were fixed to $20r_g$ and 2.5, respectively. The disk temperature of the ireflect model was assumed to be 10^5 K. The ionization parameter of the disk is defined as $\xi = 4\pi F_{\text{irr}}/n_{\text{disk}}$, where F_{irr} is the 5 eV–20 keV flux of photons irradiating the disk and n_{disk} is the gas density of the disk. Since the fraction of the reflection on the accretion disk R_{disk} and on cold matter R_{cold} are mutually dependent, they were not determined uniquely when both parameters were al-

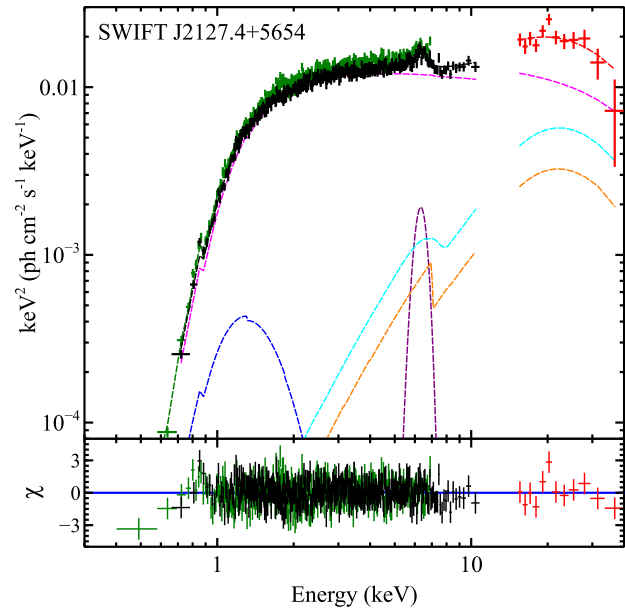


Fig. 4. Result of the spectral fit of SWIFT J2127.4+5654 with model C. The crosses and lines are the same as figure 3 and the cyan line represents the reflection component on the accretion disk.

lowed to vary. Hence, R_{cold} was fixed to 0.59, the average value of lightly obscured AGNs obtained by Kawamuro et al. (2016). We show the result of the spectral fit with the model phabs*[(1+reflect+kdblur*ireflect)*nthcomp+zgauss+zbody] (model C) in figure 4 and the best-fit parameters in table 5. The upper limit of ξ is 18 erg cm s $^{-1}$, which indicates that the ionized reflection is hardly required.

We calculate the optical depth of the corona from the results with model B for Mrk 110, IGR J16185–5928, and WKK 4438, and with model C for SWIFT J2127.4+5654. The parameter Γ

Table 5. Best-fit parameters with model C.

Model	Parameter	SWIFT J2127.4+5654
nthcomp	Γ	$2.08^{+0.05}_{-0.04}$
	kT_e (keV)	12^{+7}_{-3}
	Normalization*	$(1.2^{+0.2}_{-0.1}) \times 10^{-2}$
reflect	R_{cold}	0.59^{\dagger}
ireflect	ξ (erg cm s $^{-1}$)	< 18
	R_{disk}	$1.0^{+0.9}_{-0.7}$
zgauss	Line energy (keV)	6.38 ± 0.10
	Line width (keV)	0.4 ± 0.2
	Normalization*	$(4.6^{+1.7}_{-1.4}) \times 10^{-5}$
	Equivalent width (eV)	129^{+40}_{-45}
zbody	kT_{bb} (keV)	0.20 ± 0.02
	Normalization*	$(5.5^{+2.0}_{-2.7}) \times 10^{-5}$
	$F_{0.3-40 \text{ keV}}$ (erg cm $^{-2}$ s $^{-1}$) ‡	8.6×10^{-11}
	$L_{0.3-40 \text{ keV}}$ (erg s $^{-1}$) ‡	4.0×10^{43}
	F_{Comp} (erg cm $^{-2}$ s $^{-1}$) §	8.6×10^{-11}
	L_{Comp} (erg s $^{-1}$) §	4.0×10^{43}
	χ^2/dof	728.88/716

* in units of ph keV $^{-1}$ cm $^{-2}$ s $^{-1}$.

† fixed value.

‡ absorbed flux or luminosity in 0.3–40 keV.

§ unabsorbed flux or luminosity of the Comptonized component.

is related to the Compton y parameter with the following equation (Rybicki & Lightman 1979):

$$(\Gamma - 1)(\Gamma + 2) - \frac{4}{y} = 0. \quad (1)$$

When the corona is optically thick, the y parameter is approximated as

$$y = \frac{4kT_e}{m_e c^2} \max(\tau, \tau^2) \sim \frac{4kT_e}{m_e c^2} \tau \left(1 + \frac{\tau}{3}\right) \quad (2)$$

in the thermal Comptonization (Petrucci et al. 2001). Thus, the optical depth τ is approximated with the following equation (Sunyaev & Titarchuk 1980; Lightman & Zdziarski 1987):

$$\tau = \sqrt{\frac{9}{4} + \frac{3}{(kT_e/m_e c^2)(\Gamma - 1)(\Gamma + 2)}} - \frac{3}{2}. \quad (3)$$

The y parameter and τ are listed in table 6. The corona is found to be optically thick at least for Mrk 110 and SWIFT J2127.4+5654.

3.2 NuSTAR Analysis

We also analyzed the NuSTAR data of SWIFT J2127.4+5654 (table 2). The same data were already analyzed by Marinucci et al. (2014). They performed spectral fittings with a common value of kT_e regardless of the change in luminosity. On the other hand, as described below, the purpose of our analysis is to study the correlation between kT_e and the luminosity.

Figure 5 shows the FPMA lightcurve including background. The count rate of background was stable at

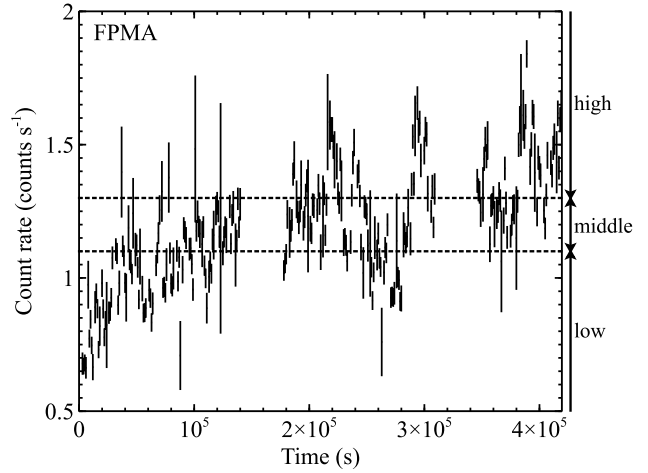


Fig. 5. Background inclusive FPMA lightcurve of SWIFT J2127.4+5654 in 3–79 keV. The x-axis represents the duration from the beginning of the observation. Each data bin has 1 ks in width.

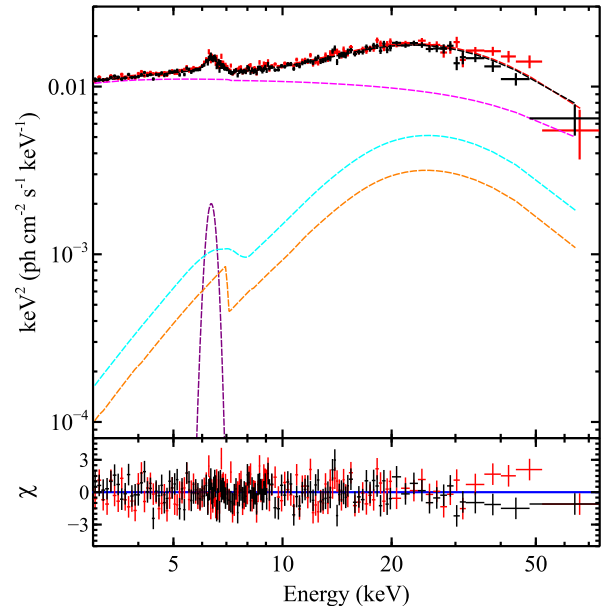


Fig. 6. Time averaged spectra of SWIFT J2127.4+5654. The black and red crosses represent FPMA and FPMB, respectively. The lines are the same as figure 4.

Table 6. Compton y parameter and τ .

Parameter	Mrk 110	SWIFT J2127.4+5654	IGR J16185–5928	WKK 4438
y	1.11 ± 0.03	$0.91^{+0.05}_{-0.06}$	$0.94^{+0.05}_{-0.03}$	$1.06^{+0.02}_{-0.03}$
τ	$6.3^{+0.4}_{-0.5}$	$4.1^{+0.8}_{-1.5}$	< 3.2	< 7.3

Table 7. Best-fit parameters of the time averaged spectra.

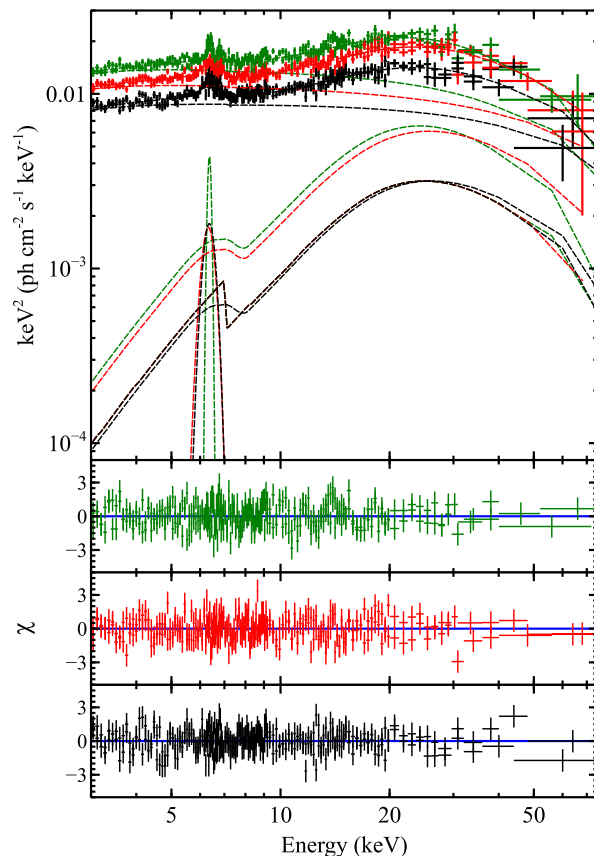
Model	Parameter	time average
nthcomp	Γ	2.05 ± 0.03
	kT_e (keV)	20^{+5}_{-2}
	Normalization*	$(1.24 \pm 0.04) \times 10^{-2}$
reflect	R_{cold}	0.59^\dagger
ireflect	ξ (erg cm s $^{-1}$)	< 22
	R_{disk}	$1.0^{+0.2}_{-0.3}$
zgauss	Line energy (keV)	6.43 ± 0.05
	Line width (keV)	0.2 ± 0.1
	Normalization*	$(2.8 \pm 0.4) \times 10^{-5}$
	Equivalent width (eV)	86^{+17}_{-11}
χ^2/dof		324.85/293

* in units of ph keV $^{-1}$ cm $^{-2}$ s $^{-1}$.

† fixed value.

about 0.04 counts s $^{-1}$. In this observation, the luminosity changed about three times from peak to peak. We first fit time averaged spectra in the 3–78 keV band with the same model as model C but without the zbody model, `phabs*[(1+reflect+kdblur*ireflect)*nthcomp+zgauss]` (see figure 6), since the soft excess is negligible above 3 keV. The seed photon temperature was fixed to $kT_{\text{bb}} = 0.1$ keV. The other parameters were fixed to the same values as used in the Suzaku analysis. The cross-normalization factor between FPMA and FPMB was allowed to vary. The best-fit parameters are shown in table 7. The ionization parameter is again constrained to be very small ($\xi < 22$ erg cm s $^{-1}$), being consistent with the Suzaku result in section 3.1. The fit gave an electron temperature of $kT_e = 20^{+5}_{-2}$ keV. It is considerably lower than that obtained with the same NuSTAR data by Marinucci et al. (2014). We consider this is due to the difference in CALDB used between the two analyses. A major update of CALDB of NuSTAR was made in 2016 June ², in which the low energy effective area of the instrument was revised based on an observation of Crab at a large off-axis angle (Madsen et al. 2017).

In order to search for possible spectral changes, we divided the FPMA and FPMB datasets according to the count rate of FPMA into three, the high, middle, and low flux periods, as shown in figure 5. We fit the spectra of the three periods with the same model as that used for the time averaged spectra. We can safely assume that the reflection component on the cold matter


Fig. 7. Spectra of SWIFT J2127.4+5654 in the high (green crosses), middle (red crosses), and low (black crosses) flux period. The dashed lines represent models.

is stable during the observation (5 days), considering the torus size (e.g., ~ 300 light-days; Kynoch et al. 2018) and its viewing solid angle ($\Omega = 1.18\pi$ when $R_{\text{cold}} = 0.59$). We used the model `phabs*[reflect*nthcomp1+(1+kdblur*ireflect)*nthcomp2+zgauss]`, in which the parameters for the reflection component on the cold matter (`reflect*nthcomp1`) were fixed to the best-fit values from the time averaged spectrum fit (table 8). We also fixed the ionization parameter for the reflection component on the inner disk (`kdblur*ireflect*nthcomp2`) to $\xi = 0$, since the contribution of the ionized reflection is found to be negligible with the time averaged spectrum. We show the results of the spectral fit in figure 7. In the high flux period, kT_e is slightly lower than those in the middle and low flux periods. Figure 8 shows the confidence contours of the mutually dependent parameters Γ and kT_e , suggesting marginal difference of the spectral shape among the three periods.

² (https://heasarc.gsfc.nasa.gov/docs/heasarc/caldb/nustar/docs/release_20160606.txt)

Table 8. Best-fit parameters of the spectra in each flux period.

Model	Parameter	high	middle	low
nthcomp ₁ [‡]	Γ	2.05 [†]	2.05 [†]	2.05 [†]
	kT_e (keV)	20 [†]	20 [†]	20 [†]
	Normalization*	1.24×10^{-2} [†]	1.24×10^{-2} [†]	1.24×10^{-2} [†]
reflect [‡]	R_{cold}	0.59 [†]	0.59 [†]	0.59 [†]
nthcomp ₂	Γ	2.06 ± 0.04	2.07 ± 0.04	$2.02^{+0.04}_{-0.03}$
	kT_e (keV)	17 ± 3	25^{+11}_{-6}	23^{+15}_{-6}
	Normalization*	$(1.56^{+0.08}_{-0.07}) \times 10^{-2}$	$(1.29^{+0.06}_{-0.07}) \times 10^{-2}$	$(0.93 \pm 0.05) \times 10^{-2}$
ireflect	ξ (erg cm s ⁻¹)	0 [†]	0 [†]	0 [†]
	R_{disk}	1.1 ± 0.3	$1.1^{+0.4}_{-0.3}$	0.7 ± 0.3
zgauss	Line energy (keV)	$6.46^{+0.07}_{-0.08}$	6.39 ± 0.10	$6.43^{+0.09}_{-0.08}$
	Line width (keV)	< 0.3	$0.3^{+0.1}_{-0.2}$	$0.3^{+0.1}_{-0.2}$
	Normalization*	$(2.2^{+0.9}_{-0.6}) \times 10^{-5}$	$(3.0^{+0.9}_{-0.8}) \times 10^{-5}$	$(2.9^{+0.8}_{-0.7}) \times 10^{-5}$
	Equivalent width (eV)	56^{+12}_{-16}	88^{+27}_{-17}	113^{+25}_{-21}
	$F_{3-78 \text{ keV}}$ (erg cm ⁻² s ⁻¹) [§]	8.1×10^{-11}	7.2×10^{-11}	5.5×10^{-11}
	$L_{3-78 \text{ keV}}$ (erg s ⁻¹) [§]	3.8×10^{43}	3.4×10^{43}	2.6×10^{43}
	F_{Comp} (erg cm ⁻² s ⁻¹)	1.2×10^{-10}	1.0×10^{-10}	7.9×10^{-11}
	L_{Comp} (erg s ⁻¹)	5.6×10^{43}	4.7×10^{43}	3.7×10^{43}
	χ^2/dof	322.20/294	302.35/294	261.12/294

* in units of ph keV⁻¹ cm⁻² s⁻¹.

† fixed value.

‡ These models represent the stable reflection component from the distant cold matter (reflect*nthcomp₁).

§ absorbed flux or luminosity in 3–78 keV.

|| unabsorbed flux or luminosity of the Comptonized component.

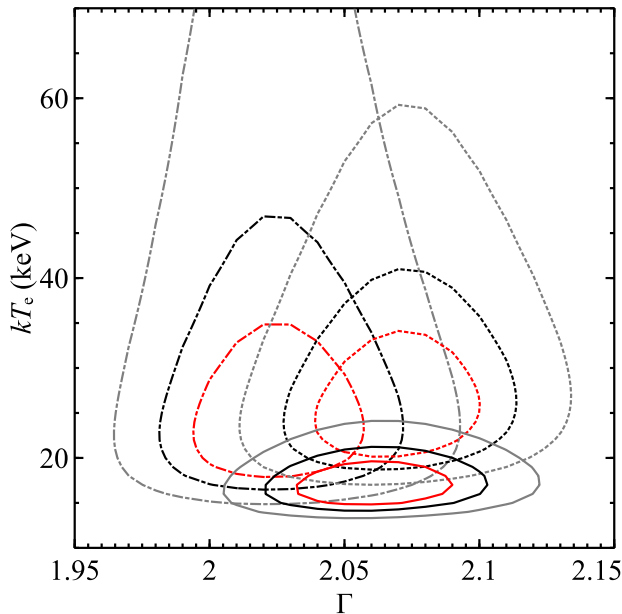


Fig. 8. Confidence contours of kT_e versus Γ in NuSTAR results of SWIFT J2127.4+5654. The solid, dotted, and dot-dashed lines correspond to the high, middle, and low flux period, and red, black, and gray lines represent 1 σ , 90%, and 99% confidence level, respectively.

4 Discussion

4.1 Comparison of the Nature of the Corona between NLS1s and BLS1s

We studied the X-ray wide band spectra of the four NLS1s. E_c of Mrk 110 is successfully constrained in this paper for the first time. E_c of SWIFT J2127.4+5654, IGR J16185–5928, and WKK 4438 obtained in this paper agree with those reported by Malizia et al. (2008), while we constrained the value with smaller error for WKK 4438. For SWIFT J2127.4+5654, E_c in our result is also consistent with those of Panessa et al. (2011) and Miniutti et al. (2009).

For BLS1s, Malizia et al. (2003) reported the average cut-off energy of $E_c = 216^{+75}_{-41}$ keV. The same group reported the mean value of $E_c = 128$ keV with a spread of 46 keV (Malizia et al. 2014). Except for IGR J16185–5928, our spectral analyses of the NLS1s gave cutoff energies of $E_c \sim 40$ keV, which are lower than those of BLS1s. This is consistent with the suggestion by Malizia et al. (2008) that NLS1s have lower E_c than BLS1s. Malizia et al. (2008) pointed out also that NLS1s have steeper spectra than BLS1s. In order to systematically study these differences between NLS1s and BLS1s, we present relation between Γ and E_c from the pexrav model fits (model A) in figure 9, together with results on BLS1s by Malizia et al. (2014). Our NLS1 sample has typically larger Γ and lower E_c than the BLS1 sample, confirming the claim by Malizia et al. (2008) that NLS1s have softer spectra and lower kT_e . The two

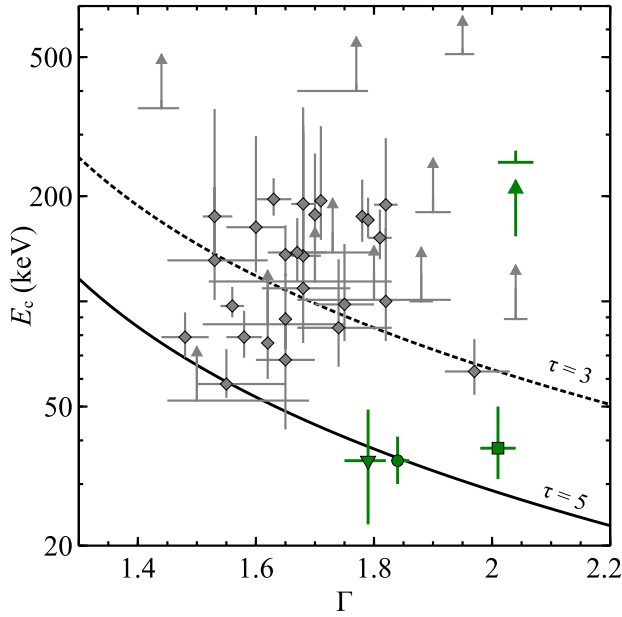


Fig. 9. Scatter plot of E_c and Γ . The green circle, square and triangle represent Mrk 110, SWIFT J2127.4+5654 and WKK 4438, respectively. The green arrow shows the lower limit obtained from IGR J16185–5928. The gray diamonds and arrows correspond to BLS1s (Malizia et al. 2014). For BLS1s, the 90% confidence range was divided by 1.645, converted to 1σ . The lower limits are at 90% confidence levels. The black lines represent equation (3) with a simple estimation as $E_c = 3kT_e$ (Petrucci et al. 2001).

parameters Γ and E_c are statistically coupled and often show a positive correlation. The correlation we found, however, is a negative one, which cannot be explained by the statistical coupling. We also found that the corona of our NLS1 sample tends to be optically thicker than that of the BLS1 sample in figure 9 (see also table 6 and Petrucci et al. 2001).

4.2 Dependence of the electron temperature on the accretion rate

Malizia et al. (2008) suggested that the accretion rate is a factor determining the electron temperature of a corona. We search for any correlation between the accretion rate and the electron temperature of our NLS1 sample. We here employ the ratio of the luminosity of seed photons entering the corona (L_{seed}) to the Eddington luminosity (L_{Edd}) to represent the accretion rate. Under the assumption that the Compton process is isotropic, a half of the up-scattered photons are emitted to the outside of the corona with a luminosity L_{Comp} , and the other half of them are emitted back to the seed photon field. The radiative equilibrium is then expressed as $L_{\text{seed}} = L_{\text{Comp}}$. Therefore, the ratio $L_{\text{seed}}/L_{\text{Edd}}$ can be regarded as being equal to $L_{\text{Comp}}/L_{\text{Edd}}$. Figure 10 shows the plot of kT_e versus $L_{\text{Comp}}/L_{\text{Edd}}$ of our NLS1 sample, where L_{Comp} was calculated from the flux of the unabsorbed $n\text{thcomp}$ model. Sources with a larger ratio $L_{\text{Comp}}/L_{\text{Edd}}$ tend to have lower kT_e in our sample. The NuSTAR results hint that this negative correlation is also seen

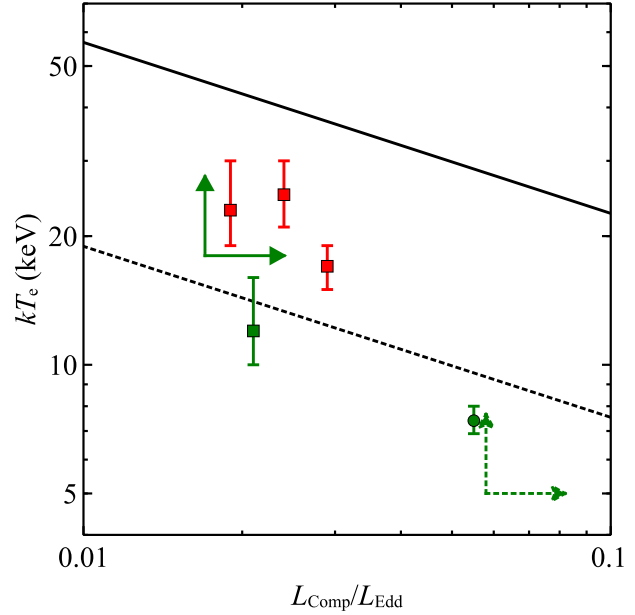


Fig. 10. Plot of kT_e versus $L_{\text{Comp}}/L_{\text{Edd}}$. Green and red correspond to the Suzaku results and NuSTAR results, respectively. Markers are the same as figure 9 but WKK 4438 is represented by dotted arrows. The lower limits of kT_e are at 90% confidence levels. The black solid line represents equation (8). The black dotted line is scaled from the black solid line by a factor of 1/3 in the y-axis direction.

in the flux variation of SWIFT J2127.4+5654.

We try to explain the trend in figure 10 by assuming that the dominant channels of electron cooling and heating are inverse Compton scattering and Coulomb collisions with protons, respectively, following a scenario proposed by Miyakawa et al. (2008), who discussed black hole binaries. Inverse Compton scattering cools electrons at a rate of

$$\left(\frac{dE}{dt}\right)_{\text{Comp}} \sim \frac{4kT_e}{m_e c^2} U_{\text{seed}} n \sigma_T, \quad (4)$$

where U_{seed} is the seed photon flux density, n is the number density of electrons, and σ_T is the Thomson scattering cross section. The photon flux density is given by $U_{\text{seed}} \simeq L_{\text{seed}}/(\pi r^2)$, where r is the radius of the corona. Electrons are heated by protons through Coulomb collisions at a rate of

$$\left(\frac{dE}{dt}\right)_{\text{Coulomb}} \sim \frac{3}{2} \frac{nkT_p}{t_{pe}}. \quad (5)$$

The relaxation time of Coulomb collisions is given by

$$t_{pe} = \left[\frac{3m_p m_e}{8(2\pi)^{\frac{1}{2}} e^4 n \ln \Lambda} \right] \left(\frac{kT_p}{m_p} + \frac{kT_e}{m_e} \right)^{\frac{3}{2}} \\ \sim \left[\frac{3m_p m_e}{8(2\pi)^{\frac{1}{2}} e^4 n \ln \Lambda} \right] \left(\frac{kT_e}{m_e} \right)^{\frac{3}{2}}, \quad (6)$$

which is the time needed for protons to establish a Maxwell distribution (Spitzer 1962). Here kT_p and m_p denote the proton temperature and the proton rest mass, respectively. The Coulomb logarithm $\ln \Lambda$ is represented by $\ln \Lambda = \ln \left\{ [3/(2e^3)] \sqrt{(kT_e)^3/(\pi n)} \right\}$. In a corona, the heating rate

should balance with the cooling rate, i.e.,

$$\frac{3}{2} \frac{nkT_p}{t_{pe}} = \frac{4kT_e}{m_e c^2} U_{seed} n \sigma_T. \quad (7)$$

If the proton energy loss rate given by equation (5) is fast enough compared to the viscous-heating rate through accretion, the proton temperature is approximately given by $kT_p \sim GMm_p/r$. As described above, L_{seed} is comparable with L_{Comp} . Thus, kT_e is represented with the ratio L_{Comp}/L_{Edd} as

$$kT_e = \left[\frac{4m_p \sigma_T}{(2\pi)^{\frac{1}{2}} e^4 m_e^{\frac{3}{2}} c \tau \ln \Lambda} \right]^{-\frac{2}{5}} \left(\frac{L_{Comp}}{L_{Edd}} \right)^{-\frac{2}{5}}, \quad (8)$$

where $\tau = nr\sigma_T$. This equation indicates that kT_e is proportional to $(L_{Comp}/L_{Edd})^{-2/5}$ despite a little fluctuation of τ and $\ln \Lambda$.

We overlay the prediction by equation (8) on our observational results plotted in figure 10. In the model calculation, we assumed $\tau = 4$ and $r = 20r_g$, which gives $n = 2 \times 10^{10} \text{ cm}^{-3}$. In spite of the simple approximations, the model curve reproduces the negative slope of kT_e as a function of L_{Comp}/L_{Edd} and agrees with the data within a factor of $\sim 2-3$. The factor of $\sim 2-3$ may indicate that some other cooling mechanisms of electrons have to be taken into account than our very simple assumptions.

5 Conclusion

We studied X-ray spectra of the four NLS1s, Mrk 110, SWIFT J2127.4+5654, IGR J16185–5928, and WKK 4438, using Suzaku and NuSTAR data. The main conclusions of our work are summarized as follows.

1. The spectra of the four sources are reproduced well with a model consisting of a cutoff power law component, a reflection component, and a soft excess component. All the four sources gave photon indices of $\Gamma \sim 2$. The cutoff energies were constrained to be $E_c \sim 40 \text{ keV}$ for Mrk 110, SWIFT J2127.4+5654, and WKK 4438 whereas a lower limit of $E_c > 155 \text{ keV}$ was obtained for IGR J16185–5928. Comparing the best-fit values of Γ and E_c with those of BLS1s by Malizia et al. (2014), we found that the NLS1s in our sample have systematically softer spectra and lower E_c than the BLS1s. Since the electron temperature is related to the cutoff energy as $E_c \approx 2-3kT_e$, our result suggests that NLS1s have lower kT_e than BLS1s.
2. We also fitted the Suzaku and NuSTAR spectra, replacing the above mentioned cutoff power law component with a thermal Comptonization model. In the case of SWIFT J2127.4+5654, from which we detected a broad Fe $K\alpha$ emission line, we took into account relativistic reflection on the accretion disk. We obtained electron temperatures of $kT_e \sim 10-20 \text{ keV}$ for Mrk 110 and SWIFT J2127.4+5654,

and lower limits of $kT_e > 18 \text{ keV}$ for IGR J16185–5928 and $kT_e > 5 \text{ keV}$ for WKK 4438. The NuSTAR results hint that kT_e in the high flux period is lower than those in the middle and low flux periods. Combining the results of the four sources, we found that kT_e anti-correlates with the ratio L_{Comp}/L_{Edd} . The anti-correlation can be explained by a simple model in which electrons in the corona are cooled and heated through inverse Compton scattering and Coulomb collisions with protons, respectively.

Acknowledgments

The authors would like to thank to all the members of the Suzaku team and the NuSTAR team. This work is supported by JSPS/MEXT Scientific Research Grant Number JP25109004 (T.T. and T.G.T.), JP15H02090 (T.G.T.), JP26610047 (T.G.T.), JP17K05384 (Y.U.), JP15H02070 (Y.T.), JP16K05296 (Y.T.), and JP23340071 (K.H.).

References

- Ai, Y. L., Yuan, W., Zhou, H., Wang, T. G., Dong, X. -B., Wang, J. G., & Lu, H. L. 2013, *AJ*, 145, 90
- Arnaud, K. A. 1996, *ASP Conf. Ser.*, 101, 17
- Baumgartner, W. H., Tueller, J., Markwardt, C., & Skinner, G. 2010, *Bulletin of the American Astronomical Society*, 42, 675
- Boldt, E. A. 1987, *NASA Conference Publication*, 2464, 339
- Done, C., Davis, S. W., Jin, C., Blaes, O., & Ward, M. 2012, *MNRAS*, 420, 1848
- Done, C., Jin, C., Middleton, M., & Ward, M. 2013, 434, 1995
- Fabian, A. C., Rees, M. J., Stella, L., & White, N. E. 1989, *MNRAS*, 238, 729
- Fukazawa, Y., et al. 2009, *PASJ*, 61, 17
- George, I. M., & Fabian, A. C. 1991, *MNRAS*, 249, 352
- Haardt, F., Maraschi, L., & Ghisellini, G. 1994, *ApJ*, 432, L95
- Harrison, F. A., et al. 2013, *ApJ*, 770, 103
- Jin, C., Ward, M., Done, C., & Gelbord, J. 2012, *MNRAS*, 420, 1825
- Kalberla, P. M. W., Burton, W. B., Hartmann, Dap, Arnal, E. M., Bajaja, E., Morras, R., & Pöppel, W. G. L. 2005, *A&A*, 440, 775
- Kara, E., García, J. A., Lohfink, A., Fabian, A. C., Reynolds, C. S., Tombesi, F., & Wilkins, D. R. 2017, *MNRAS*, 468, 3489
- Kawamuro, T., Ueda, Y., Tazaki, F., Ricci, C., & Terashima, Y. 2016, *ApJS*, 225, 14
- Kokubun, M., et al. 2007, *PASJ*, 59, 53
- Kollatschny, W. 2004, *IAUS*, 222, 105
- Koyama, K., et al. 2007, *PASJ*, 59, 23
- Kynoch, D., et al. 2018, *MNRAS*, 475, 404
- Laor, A. 1991, *ApJ*, 376, 90
- Lighrman A. P. & Zdziarski A. A., 1987, *ApJ*, 319, 643
- Madsen, K. K., Forster, K., Grefenstette, B. W., Harrison, F. A., & Stern, D. 2017, *ApJ*, 841, 56
- Magdziarz, P., & Zdziarski, A. A. 1995, *MNRAS*, 273, 837
- Malizia, A., Bassani, L., Stephen, J. B., Di Cocco, G., Fiore, F., & Dean, A. J. 2003, *ApJ*, 589, L17
- Malizia, A., et al. 2008, *MNRAS*, 389, 1360
- Malizia, A., Molina, M., Bassani, L., Stephen, J. B., Bazzano, A., Ubertini, P., & Bird, A. J. 2014, *ApJ*, 782, L25

- Marinucci, A., et al. 2014, *MNRAS*, 440, 2347
- Masetti, N., et al. 2006 *A&A*, 459, 21
- Miniutti, G., Panessa, F., de Rosa, A., Fabian, A. C., Malizia, A., Molina, M., Miller, J. M., & Vaughan, S. 2009, *MNRAS*, 398, 255
- Mitsuda, K., et al. 2007, *PASJ*, 59, 1
- Miyakawa, T., Yamamoto, K., Homan, J., Saito, K., Dotani, T., Yoshida, A., & Inoue, H. 2008, *PASJ*, 60, 637
- Osterbrock, D. E., & Pogge, R. W. 1985, *ApJ*, 297, 166
- Ozawa, M., et al. 2009, *PASJ*, 61, S1
- Panessa, F., et al. 2011, *MNRAS*, 417, 2426
- Patrick, A. R., Reeves, J. N., Porquet, D., Markowitz, A. G., Lobban, A. P., & Terashima, Y. 2011, *MNRAS*, 411, 2355
- Petrucci, P. O. et al. 2001, *ApJ*, 556, 716
- Petrucci, P. O. et al. 2013, *A&A*, 549, A73
- Ross, R. R., & Fabian, A. C. 1993, *MNRAS*, 261, 74
- Rybicki, G. B., & Lightman, A. P. 1979, (New York, Wiley-Interscience), ch. 7
- Spitzer, L. 1962, *Physics of Fully Ionized Gases* (New York: Wiley)
- Sunyaev, R. A., & Titarchuk, L. G. 1980, *A&A*, 86, 121
- Takahashi, T., et al. 2007, *PASJ*, 59, 35
- Tortosa, A., et al. 2018, *MNRAS*, 473, 3104
- Uchiyama, H., et al. 2009, *PASJ*, 61, 9
- Zdziarski, A. A., Johnson, W. N., & Magdziarz, P. 1996, *MNRAS*, 283, 193
- Życki, P. T., Done, C., & Smith, D. A. 1999, *MNRAS*, 309, 561